

## Full counting statistics of the two-stage Kondo effect

D. B. Karki<sup>1,2</sup> and Mikhail N. Kiselev<sup>1</sup>

<sup>1</sup>*The Abdus Salam International Centre for Theoretical Physics (ICTP), Strada Costiera 11, I-34151 Trieste, Italy*

<sup>2</sup>*International School for Advanced Studies (SISSA), Via Bonomea 265, 34136 Trieste, Italy*



(Received 24 August 2018; published 29 October 2018)

We developed a theoretical framework which extends the method of full counting statistics (FCS) from conventional single-channel Kondo screening schemes to a multichannel Kondo paradigm. The developed idea of FCS has been demonstrated considering an example of a two-stage Kondo (2SK) model. We analyzed the charge-transferred statistics in the strong-coupling regime of a 2SK model using a nonequilibrium Keldysh formulation. A bounded value of the Fano factor,  $1 \leq F \leq 5/3$ , confirmed the crossover regimes of charge-transferred statistics in the 2SK effect, from Poissonian to super-Poissonian. An innovative way of measuring the transport properties of the 2SK effect, by the independent measurements of charge current and noise, has been proposed.

DOI: [10.1103/PhysRevB.98.165443](https://doi.org/10.1103/PhysRevB.98.165443)

### I. INTRODUCTION

Quantized charge in nanoscale systems results in large current fluctuations [1]. In addition, thermal fluctuations are ubiquitous at finite temperature. These fluctuations are prevalently measured by charge current and its noise, the first and second cumulants of fluctuating current [2]. The study of noise in a generic nanodevice provides underlying transport information that cannot be inferred from the average current measurements [1–8]. In particular, noise measurement imparts an effective way of probing the dynamics of charge transfer [2,8]. Moreover, noise has revealed the nature of quasiparticle interactions and different types of entanglements associated with the system [9–11]. In addition to first and second cumulants of the fluctuating current, the fundamental relevance of higher-order cumulants to describe the transport processes in nanostructures has been also demonstrated [9,12–19].

The method of full counting statistics (FCS) furnishes an elegant way to scrutinize an *arbitrary-order* ( $n$ th-order) cumulant of current through a nanodevice [3–5]. The probabilistic interpretation of charge transport is at the core of FCS theory. The primary object of FCS is the moment-generating function (MGF) for the probability distribution function (PDF) of transferred charges within a given time interval [3–5]. The moments of PDF of order  $n \geq 2$  characterize the current fluctuations. The FCS scheme permits in this way a transparent study of the quantum transport in various nanostructures. Notably, FCS of normal metal-superconductor hybrid structures, superconducting weak links, tunnel junctions, chaotic cavities, entangled electrons, spin-correlated systems, charge shuttles, and nanoelectromechanical systems are the most striking examples [20–27].

In nanoscale transport studies, an archetype of an electronic device consists of an impurity sandwiched between two reservoirs of conduction electrons [1,2]. The artificial atom, molecule, quantum dot (QD), carbon nanotube (CNT), etc., plays the role of an impurity. Given their low tunneling rate, the QDs represents archetypal setups for the study of a highly accurate FCS [28], the main concern of the present work. The

transport through the QD depends strongly on the associated number of electronic levels, while the orbitals of the impurity play the major role in defining the underlying transport characteristics [29]. Out of all the impurities-mediated transport processes, those with intrinsic magnetic moment, and hence those that are magnetic in nature, have attracted ever-increasing interests [29,30]. One can expect variant transport fingerprints when such magnetic impurities exchange coupled to conduction electrons (for review see Ref. [31]).

In the low-energy regime of transport measurements, the correlation between the localized spin of the impurity and the spin of conduction electrons results in the well-known many-body phenomenon, the Kondo screening effect [32]. The fundamental role of the Kondo effect in enhancing and controlling the transport through a nanostructure is the acknowledged evidence [33–44]. In a transport setup with two reservoirs (leads), the Kondo screening of the localized spin is caused by at most two conduction channels, the symmetric and antisymmetric combination of electron states in the leads. The interplay between the number of conduction channels ( $\mathcal{K} = 1, 2$ ) and the effective spin of the magnetic impurity ( $\mathcal{S} \geq 1/2$ ) boosts further the richness of Kondo physics. Specifically,  $\mathcal{K} = 2\mathcal{S}$  put forward the controllable comprehension of Kondo effects in nanodevices [45]. In this particular case, the effective spin of the impurity gets completely screened by the spin of the conduction electrons. Such fully screened Kondo effects are of immense interest given their low-energy behavior described by a local Fermi-liquid (FL) theory [33–35].

The Kondo screening involving only a single channel of conduction electrons ( $\mathcal{K} = 1$ ) and a spin half impurity ( $\mathcal{S} = 1/2$ ) forms a prototypical example of the fully screened Kondo effect. The magnetic impurities with only one orbital manifest the single-channel Kondo (1CK) effect. Tremendous perseverance [45–48] has been devoted to understanding the transport behavior in paradigmatic 1CK schemes. Moreover, various seminal works [49–54] paved the way to access the associated FCS in the 1CK realm. Unlike the 1CK effect, the transport characteristics of a multiorbital impurity have

been less explored. In this facet, many orbitals of the conduction channels are involved in screening the impurity spin (multichannel screening), which makes the problem more obscure [55]. Nonetheless, several cogent evidences [55–59], theoretical and experimental, are available to demonstrate the relevance of the multichannel screening effect in a generic transport setup. The simplest multichannel screening involves two conduction channels ( $\mathcal{K} = 2$ ) and  $S \geq 1/2$ : the general manifestation of a two-lead geometry. In the present work we focus only on the particular case of multichannel screening such that  $\mathcal{K} = 2S$  in a two-lead setup. Thus the  $S = 1$  impurity interacting with two channels of conduction electrons forms the minimal description of multichannel screening in the FL regime [60,61].

A multiorbital quantum impurity with effective spin  $S = 1$  connected to two terminals can lead to a Kondo effect exhibiting two-stage screening [61]. The first-stage screening process involves an underscreened Kondo effect where the impurity spin is effectively reduced from  $S = 1$  to  $S = 1/2$ . Subsequently, second-stage screening leads to complete screening of the impurity spin and the formation of a Kondo singlet. This feature of screening is called the two-stage Kondo (2SK) effect [55,60]. The low-energy description of such 2SK effects is still governed by a local FL theory. Nonetheless, transport properties of such FLs get modified in dramatic ways compared to the 1CK effect [61]. The strong interplay between two conduction channels, both close to resonance scattering, causes the aforesaid different transport features over the 1CK effect. The lack of a compatible cure for the two Kondo resonances has made the 2SK paradigm far from being trivial for several years [55,60,62]. To analyze the equilibrium and nonequilibrium transport properties of a generic 2SK effect, a two-color local FL theory was recently developed [61]. Here, the absence of a zero-bias anomaly and the nonmonotonicity of FL transport coefficients are demonstrated as the hallmarks of the 2SK effect.

These two traits of the 2SK effect, in contrast with the 1CK effect, have raised many fascinating concerns, for instance, how these fingerprints can affect the higher cumulants of charge current, particularly the noise-to-signal ratio. This ratio is commonly known as the Fano factor ( $F$ ). The zero-temperature limit of  $F$  is of extreme experimental interest [47,63]. In the theoretical perspective, the method of FCS pertaining to the two resonance channels of conduction electrons has not been developed yet.

In this work we take the important step of revealing the FCS for the 2SK effect. The structure of this paper is as follows. The basis description of the 2SK effect setup and model Hamiltonian are given in Sec. II. We present the theory of FCS for two resonance channels of a local FL in Sec. III. Section IV is devoted to discussing the results of applying the many-body method of FCS developed in Sec. III to the 2SK model of Sec. II. Conclusions and future perspectives are presented in Sec. V. Details of mathematical calculations are given in the Appendixes.

## II. SETUP AND MODEL HAMILTONIAN

The cartoon representing the generic 2SK effect is as shown in the top panel of Fig. 1. The generic quantum

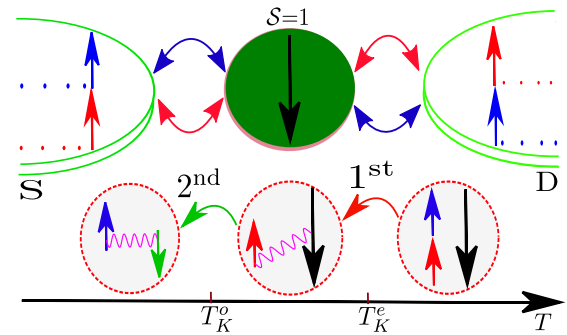


FIG. 1. Top: Schematic representation of a generic 2SK effect setup. The effective spin  $S = 1$  impurity is tunnel-coupled with two external leads, the source S and the drain D. Bottom: Flow diagram of the 2SK model from weak to strong coupling. For the entries in the figure and their explanations see Sec. II.

impurity sandwiched between two conducting leads (the source S and the drain D) is described by the Anderson model with the Hamiltonian

$$H_A = \sum_{k\alpha\sigma} \xi_k c_{\alpha k\sigma}^\dagger c_{\alpha k\sigma} + \sum_{\alpha k i\sigma} t_{\alpha i} c_{\alpha k\sigma}^\dagger d_{i\sigma} + \text{H.c.} \\ + \sum_{i\sigma} \varepsilon_i d_{i\sigma}^\dagger d_{i\sigma} + E_c \hat{N}^2 - \mathcal{J} \hat{S}^2. \quad (1)$$

The conducting leads are described by the first term of Eq. (1) such that the operator  $c_{\alpha k\sigma}^\dagger$  creates an electron with momentum  $k$  and spin  $\sigma = \uparrow(+), \downarrow(-)$  in the  $\alpha$  ( $\alpha = S, D$ ) lead. Here  $\xi_k$  is the energy of conduction electrons with respect to the chemical potential  $\mu$ . The operator  $d_{i\sigma}$  describes electrons with energy  $\varepsilon_i$  and spin  $\sigma$  in the  $i$ th orbital state of the quantum impurity. The tunneling matrix elements are represented by  $t_{\alpha i}$ , the charging energy of the impurity (dot) is  $E_c$ , and  $\mathcal{J} \ll E_c$  is an exchange integral accounting for the Hund rule [62]. The total number of electrons in the dot is given by an operator  $\hat{N} = \sum_{i\sigma} d_{i\sigma}^\dagger d_{i\sigma}$ . The two electrons in the dot ensure the expectation value of  $\hat{N}$  to be  $\bar{n}_d = 2$  and the total spin  $S = 1$ . Application of the Schrieffer-Wolff transformation [64] to the Hamiltonian Eq. (1) results in the effective Kondo Hamiltonian for the spin-1 quantum impurity [45,62].

To proceed with the calculation of FCS relevant to the setup in Fig. 1, we assume that the thermal equilibrium is maintained in source and drain, separately, at temperature  $T$ . The chemical potentials of the source and drain electrodes are  $\mu_S$  and  $\mu_D$ , respectively. The applied voltage bias across the source and drain drives the impurity-leads system out of equilibrium. For the sake of simplicity, we consider symmetrically applied bias voltage such that  $\mu_S - \mu_D = eV$ , where  $e$  is the electronic charge. In this frame, the symmetrical (even,  $e$ ) and antisymmetrical (odd,  $o$ ) combinations of electron operators in the two leads interact with the impurity. Assuming  $c_{S/D}$  as an operator that annihilates an electron in the source or drain, the even/odd combinations of electron operators are  $b_{e/o} = (c_S \pm c_D)/\sqrt{2}$ . These states are also known as conduction channels. In Fig. 1, we used arrows with different colors to show that the electrons form even and odd channels ( $\uparrow$ , electron forms channel  $e$ ;  $\downarrow$ , electron forms channel  $o$ ). Likewise, the interaction between even (odd) channel and

impurity is represented by a two-headed arrow with in blue (red). In our convention, blue (red) is generic for the even (odd) channel.

In the conventional 1CK effect the odd channel is completely decoupled from the impurity [33]. The interacting channel, the even one, is characterized by the Kondo temperature  $T_K^e$ . Depending upon the applied bias  $eV$  and the temperature  $T$  in a particular setup, different coupling regimes come into play, namely,  $(eV, T) \leq T_K^e$ , the strong-coupling regime, and  $(eV, T) \geq T_K^e$ , the weak-coupling regime. Immense efforts, experimental inclusive of theory, have been put forth for the transport description of the 1CK effect in both of the above regimes (see Refs. [29,45] for review).

In the two-lead setup with a generic quantum impurity having more than one orbital, nonetheless, neither of the electron combinations remains decoupled from the impurity [55,60]. Consequently, both of the conduction channels take part in the screening of localized spin of the impurity. In addition to  $T_K^e$ , another energy scale characterizing the Kondo temperature of the odd channel,  $T_K^o$ , is used to engage the problem of the 2SK effect. The interplay between two Kondo temperatures ( $T_K^a$ ,  $a = e, o$ ) makes the 2SK problem far richer than the 1CK problem, but at the same time notoriously difficult. Perturbation treatments of weak,  $(eV, T) > \max(T_K^e, T_K^o)$ , and intermediate,  $T_K^o \leq (eV, T) \leq T_K^e$ , coupling regimes have been formulated [60,62]. In the intermediate regime the impurity spin gets partially screened via first-stage screening. Still swapping the temperature and bias voltage down, to satisfy the condition  $(eV, T) \ll \min(T_K^e, T_K^o)$ , results in the strong-coupling regime of the 2SK effect. In this second stage the complete screening of the impurity spin is achieved. These three coupling regimes are shown in the bottom panel of Fig. 1.

Furthermore, it has been argued [55,60] that the most nontrivial part of the 2SK effect is the strong-coupling regime, where both of the interacting channels are close to the resonance scattering. Since the 2SK effect satisfies the identity  $\mathcal{K} = 2\mathcal{S}$ , it offers the transport description in terms of a local FL. From now on, we focus only on the strong-coupling regime of the 2SK effect. Owing to its low-energy behavior as a local FL, we describe the strong-coupling regime of the 2SK effect in the spirit of Nozières's FL theory [33,35]. Accordingly, the Kondo singlet (Kondo cloud) acts as the scatterer for the incoming electrons from the leads. Outgoing and incoming electrons then differ from each other by the phase shifts  $\delta_\sigma^a(\varepsilon)$ . At low energy,  $\varepsilon \ll \min(T_K^e, T_K^o)$ , we expand the phase shifts in terms of phenomenological parameters to write [33]

$$\delta_\sigma^a(\varepsilon) = \delta_0^a + \alpha_a \varepsilon - \phi_a \delta N_\sigma^a + \Phi \sigma (\delta N_\uparrow^a - \delta N_\downarrow^a). \quad (2)$$

Here,  $\delta_0^a = \pi/2$  are the resonance phase shifts considered to be the same for both channels and both spin components. Writing Eq. (2) we explicitly consider the particle-hole (p-h) symmetric limit:  $\sigma = \uparrow, \downarrow$  ( $\bar{\sigma} = \downarrow, \uparrow$ ). The first two terms of Eq. (2) represents the purely elastic effects associated with the two channels. These are, equivalently, known as the scattering terms. The parameters  $\alpha_a$  are the Nozières FL coefficients characterizing the scattering. Although for  $\varepsilon = T = eV = 0$  both channels are at resonance, the way the phase shifts changes with energy is different in the two channels. This

consequence can be accounted for by defining the Kondo temperature as [48,65]

$$T_K^a = 1/\alpha_a. \quad (3)$$

For definiteness, we consider  $T_K^o \leq T_K^e$  throughout the paper.

In addition, the third and fourth terms of Eq. (2) are due to the finite inelastic effects. These are known as interaction terms. The parameters  $\phi_a$  quantify the intrachannel interactions, and the interchannel interaction is accounted for by  $\Phi$ . The notation  $\delta N_\sigma^a$  is defined by

$$\delta N_\sigma^a = \int_{-\infty}^{\infty} [\langle b_{a\varepsilon\sigma}^\dagger b_{a\varepsilon\sigma} \rangle_0 - \Theta(\varepsilon_F - \varepsilon)] d\varepsilon.$$

Here,  $\varepsilon_F$ , in the argument of step function  $\Theta$ , is the Fermi energy. The average  $\langle \cdot \rangle_0$  is taken with respect to the non-interacting Hamiltonian describing the free electrons in two channels,

$$H_0 = \nu \sum_{a\sigma} \int_{\varepsilon} \varepsilon b_{a\varepsilon\sigma}^\dagger b_{a\varepsilon\sigma}, \quad (4)$$

where  $\nu$  is the density of states per species for a one-dimensional channel. We see that the phase-shift expression, Eq. (2), consists of five FL parameters ( $\alpha_e, \alpha_o, \phi_e, \phi_o$ , and  $\Phi$ ). However, the invariance of phase shifts under the shift of reference energy (the floating of the Kondo resonance [47]) recovers the FL identity  $\alpha_a = \phi_a$ . Thereupon, three independent FL parameters ( $\alpha_e, \alpha_o$ , and  $\Phi$ ) completely describe the low-energy sector of the 2SK problem. With the specification of  $T_K^a$  in terms of  $\alpha_a$  as in Eq. (3), we have only one FL parameter ( $\Phi$ ) to relate with the physical observables. The response function measurements could provide a way to access the parameter  $\Phi$  [61]. Therefore, all the phenomenological parameters in Eq. (2) are under control in an experiment.

On theoretical grounds, the finding of the seminal work of Ref. [35] paved the way to formulate the Hamiltonian describing the scattering and interaction processes in Eq. (2). The p-h symmetry of the problem demands the scattering terms to be represented by the Hamiltonian

$$H_{el} = -\frac{\alpha_a}{2\pi} \sum_{a\sigma} \int_{\varepsilon_{1-2}} (\varepsilon_1 + \varepsilon_2) b_{a\varepsilon_1\sigma}^\dagger b_{a\varepsilon_2\sigma}. \quad (5)$$

Similarly, the intrachannel and interchannel quasiparticle interactions are designated by the Hamiltonians  $H_\phi$  and  $H_\Phi$ , respectively, where  $H_{in} = H_\phi + H_\Phi$  represents the total interactions associated with the 2SK effect. Here,

$$H_\phi = \frac{\phi_a}{2\pi\nu} \sum_{a\sigma} \int_{\varepsilon_{1-4}} : \rho_{\varepsilon_1\varepsilon_2\sigma}^a \rho_{\varepsilon_3\varepsilon_4\bar{\sigma}}^a :, \quad (6)$$

$$H_\Phi = -\frac{\Phi}{2\pi\nu} \sum_{\sigma_{1-4}} \int_{\varepsilon_{1-4}} : S_{\varepsilon_1\varepsilon_2\sigma_1\sigma_2}^o S_{\varepsilon_3\varepsilon_4\sigma_3\sigma_4}^e :, \quad (7)$$

The notation  $:\dots:$  denotes the normal ordering. In Eqs. (6) and (7) we used the short-hand notation

$$\rho_{\varepsilon_1\varepsilon_2\sigma}^a \equiv b_{a\varepsilon_1\sigma}^\dagger b_{a\varepsilon_2\sigma}, \quad S_{\varepsilon_1\varepsilon_2\sigma_1\sigma_2}^a \equiv b_{a\varepsilon_1\sigma_1}^\dagger \tau_{\sigma_1\sigma_2} b_{a\varepsilon_2\sigma_2},$$

with  $\tau_{\sigma_i\sigma_j}$  the elements of Pauli-matrices. The scattering and interaction parts of the Hamiltonian given in Eqs. (5)–(7) are first order in  $1/T_K^a$ . The two-leg vertex  $\alpha_a$  and the four-leg vertices  $\phi_a$  and  $\Phi$  are shown in Fig. 2. In general the symmetry

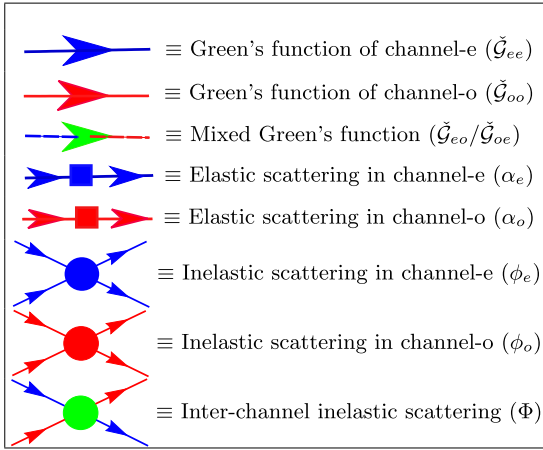


FIG. 2. Feynman diagrammatic codex used for the calculation of FCS in the presence of two conduction modes.

of the problem also allows one to construct the Hamiltonian with an eight-leg vertex, for instance,  $\tilde{\mathcal{H}} \propto \tilde{\phi}(\rho_\sigma \rho_{\bar{\sigma}})^a (\rho_\sigma \rho_{\bar{\sigma}})^{\bar{a}}$ . Note that in the present work we restrict ourselves to the second-order correction to the statistics of the charge current; thus the relevant terms are up to  $O(T/T_K^a)^2$ . Since the vertex  $\tilde{\phi}$  is already second order in  $1/T_K^a$ , it does not contribute to the cumulants of charge current within the second-order perturbative calculation and hence has been neglected. Thus the Hamiltonian  $H \equiv H_0 + H_{el} + H_{in}$  constitutes the minimal model Hamiltonian of a generic 2SK effect. This particular model has channel symmetry at the point  $\alpha_e = \alpha_o$  and  $\alpha_a = 3/2\Phi$ , where the conductance vanishes due to the destructive interference between two interacting channels [61]. It is worth noting that the effects of breaking p-h symmetry can be accounted for by introducing extra first and second generations of FL coefficients into Eq. (2) in the spirit of Ref. [47]. The  $n$ th generation of FL coefficients refers to the  $n$ th-order coefficients in the Taylor expansion of the scattering phase shifts with respect to the energy. Moreover, for the description of FCS beyond the p-h symmetric point, the density-density interchannel interaction should be added. The finite potential scattering amounts to renormalizing the resonance phase shifts in such a way that  $\delta_0^a \rightarrow \delta_0^a + \delta_p^a$ ,  $\delta_p^a \ll \delta_0^a$  [65].

### III. FULL COUNTING STATISTICS

The randomness of transferred charge ( $q$ ) through a nanodevice during a measurement time ( $\mathcal{T}$ ) is specified by the PDF,  $\mathcal{P}(q)$ . Then, the central object of FCS, the MGF, is given by

$$\chi(\lambda) = \sum_q \mathcal{P}(q) e^{i\lambda q}. \quad (8)$$

Here,  $\lambda$  is the charge counting field. Following the spirit of pioneering works [49,50], we conceal the 2SK many-body Hamiltonian into the MGF (see text below). The complete charge-transferred statistics of the 2SK effect is, then, obtained via the CGF  $\ln \chi(\lambda)$ . The  $n$ th-order differentiation of CGF with respect to the counting field delivers the arbitrary moment (central) of charge current. In addition, the counting field,  $\lambda$ , is explicitly time dependent, which takes different

values in forward ( $\mathcal{C}_-$ ) and backward ( $\mathcal{C}_+$ ) Keldysh contours:

$$\lambda(t) = \begin{cases} \lambda, & \text{if } 0 < t < \mathcal{T} \text{ and } t \in \mathcal{C}_- \\ -\lambda, & \text{if } 0 < t < \mathcal{T} \text{ and } t \in \mathcal{C}_+ \\ 0, & \text{else.} \end{cases} \quad (9)$$

Here the Keldysh contour extends from  $-\infty$  to  $\mathcal{T}$  and back to  $\infty$ . Note that, in order to calculate the FCS, the current measurement device has to be included in the Hamiltonian description. Such terms in the Hamiltonian due to the measuring device can be eliminated by means of unitary transformation of the form  $U \sim e^{-i\lambda(t)\hat{N}_\alpha}$ ,  $\hat{N}_\alpha$  being the number operator of the electrons in the  $\alpha$  reservoir [50]. This transformation changes only the tunneling part of the Hamiltonian Eq. (1). Analogously, in the strong-coupling regime the charge-measuring field causes the rotation of the even and odd electron states in the reservoirs such that [49]

$$b_a^\lambda = \cos(\lambda/4)b_a - i \sin(\lambda/4)b_{\bar{a}}. \quad (10)$$

Where, for simplicity, we omit the spin degrees of freedom. Under this transformation the free part of the Hamiltonian,  $H_0$ , remains unchanged. Nevertheless, the Hamiltonian corresponding to the sum of scattering and interaction effects,  $\mathcal{H} (\equiv H_{el} + H_{in})$ , transforms to  $\mathcal{H}^\lambda = \mathcal{H} + \lambda/4 \hat{I}_{bs}$ . Here, we considered only the lowest-order terms in the counting field. The backscattering current,  $\hat{I}_{bs}$ , is given by the commutator  $\hat{I}_{bs} = i[Q, H]$ , where  $Q$  is the charge-transferred operator across the junction  $Q = 1/2 \sum_{k\sigma} (b_{ek\sigma}^\dagger b_{ok\sigma} + \text{H.c.})$ . Since there are no zero-order transmission processes in the 2SK process [61], the MGF is given by

$$\chi(\lambda) = \left\langle T_C \exp \left[ -i \int_C \mathcal{H}^\lambda(t) dt \right] \right\rangle_0, \quad (11)$$

where  $T_C$  is the time ordering operator in the Keldysh contour  $C$ . The expansion of Eq. (11) in  $\mathcal{H}^\lambda$  and the use of Wick's theorem paved the way to proceed with the perturbative study of the MGF,  $\chi(\lambda)$ . Then the  $n$ th-order (arbitrary) moment of charge current is given by

$$C_n = \frac{1}{\mathcal{T}} (-i)^n \left. \frac{d^n}{d\lambda^n} \ln \chi(\lambda) \right|_{\lambda=0}. \quad (12)$$

To proceed with the calculation for the higher cumulants of the charge current, we require Keldysh Green's functions (GFs) in  $\lambda$ -rotated basis. As the odd conduction channel remains completely decoupled, the Keldysh GFs of the even channel ( $\check{\mathcal{G}}_{ee}$ ) suffice to characterize the transport of 1CK schemes. However, the persistent treatment of the 2SK effect requires two additional Keldysh GFs, the Keldysh GFs of the odd channel ( $\check{\mathcal{G}}_{oo}$ ) and that of the mixed channel ( $\check{\mathcal{G}}_{eo/oe}$ ). Note that the spin index in these GFs is implied. In addition, we prefer the renaming of GFs  $\check{\mathcal{G}}_{ee}$  and  $\check{\mathcal{G}}_{oo}$  as the channel-diagonal GFs, and  $\check{\mathcal{G}}_{eo/oe}$  as mixed GFs, whenever necessary. The energy representation of these Keldysh GFs is

$$\check{\mathcal{G}}_{aa/a\bar{a}}(\varepsilon) = \begin{bmatrix} \mathcal{G}_{aa/a\bar{a}}^{--}(\varepsilon) & \mathcal{G}_{aa/a\bar{a}}^{+-}(\varepsilon) \\ \mathcal{G}_{aa/a\bar{a}}^{+-}(\varepsilon) & \mathcal{G}_{aa/a\bar{a}}^{++}(\varepsilon) \end{bmatrix}, \quad (13)$$

where the diagonal GFs,

$$\mathcal{G}_{aa/a\bar{a}}^{--}(\varepsilon) = \mathcal{G}_{aa/a\bar{a}}^{++}(\varepsilon) = i\pi v[(f_S - 1/2) \pm (f_D - 1/2)], \quad (14)$$

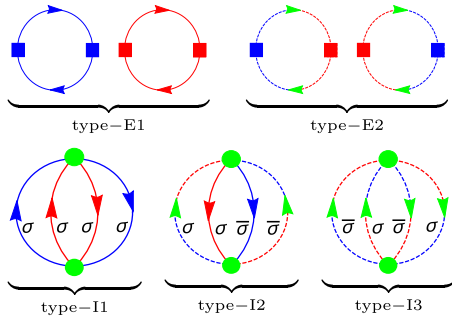


FIG. 3. Top: Schematic representation of the CGF contribution of scattering effects,  $\ln \chi_{\text{el}}(\lambda)$ . Bottom: Topologically different diagrams accounting for the interaction contribution to the CGF,  $\ln \chi_{\text{in}}(\lambda)$ .

are independent of the counting field  $\lambda$ . Here,  $f_{S/D} \equiv f_{S/D}(\varepsilon)$  is the free-electron Fermi distribution function of source/drain reservoir. The off-diagonal GFs, explicitly dependent on  $\lambda$ , are given by

$$\mathcal{G}_{aa/a\bar{a}}^{+-}(\varepsilon) = e^{i\lambda/2}(f_S - 1) \pm e^{-i\lambda/2}(f_D - 1), \quad (15)$$

$$\mathcal{G}_{aa/a\bar{a}}^{-+}(\varepsilon) = e^{-i\lambda/2}f_S \pm e^{i\lambda/2}f_D. \quad (16)$$

The pictorial representation of these GFs is shown in Fig. 2. Neither of the above GFs included the principal parts, since they do not contribute to the local quantities in the flat-band model [49]. The Fourier transformation (FT) of Eq. (16) into real time permits

$$\mathcal{G}_{aa/a\bar{a}}^{-+}(t) = \mp \pi \nu T \frac{e^{i(\frac{\lambda}{2} + \frac{eV}{2}t)} \pm e^{-i(\frac{\lambda}{2} + \frac{eV}{2}t)}}{2 \sinh(\pi T t)}. \quad (17)$$

The singularity in Eq. (17) is removed by shifting the contour of integration upward from the origin such that  $t \rightarrow t + i\eta$  for  $\eta \rightarrow 0$ . The GF  $\mathcal{G}^{+-}(t)$  has the analogous expression  $\mathcal{G}^{-+}(t)$  [52].

We substitute the scattering (elastic) part of the Hamiltonian,  $H_{\text{el}}$ , into Eq. (11) and use Wick's theorem to get the elastic contribution to the CGF,  $\ln \chi_{\text{el}}(\lambda)$ . Following the diagrammatic codex of Fig. 2, we succeed in reexpressing  $\ln \chi_{\text{el}}(\lambda)$  in terms of two topologically different Feynman diagrams. These diagrams are classified as type E1 and type E2 (see top panel of Fig. 3). Following the standard technique of Feynman diagrammatic calculation with the GFs given in Eqs. (14)–(16), we obtained the CGF contribution of type-E1 and type-E2 diagrams. As detailed in Appendix A, the CGF for the 2SK effect contributed by the scattering effects is

$$\frac{\ln \chi_{\text{el}}}{(\alpha_e - \alpha_o)^2} = \frac{TV}{24\pi} \frac{V^2 + 4(\pi T)^2}{\sinh(V/2T)} \sum_{x=\pm} (e^{-i\lambda x} - 1) e^{xV/2T}. \quad (18)$$

We have used the generalized notation  $e = \hbar = k_B = 1$  to write Eq. (18) and for the rest of the discussion. Plugging Eq. (18) into Eq. (12) and then taking the limit  $T \rightarrow 0$ , we bring the zero-temperature contribution of scattering effects

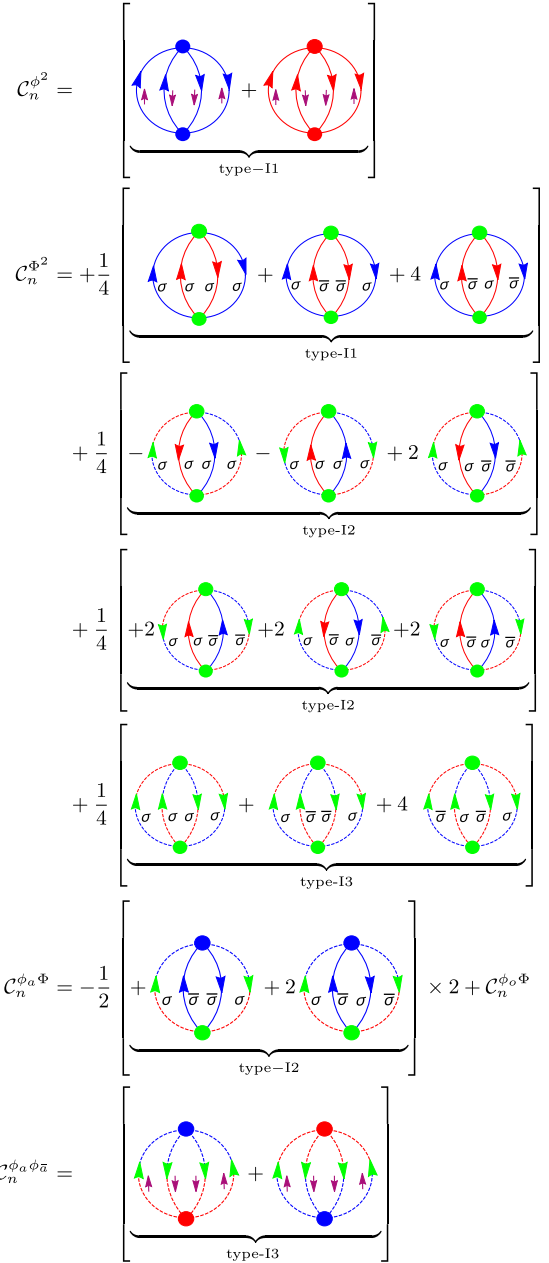


FIG. 4. Feynman diagrams representing the second-order interaction corrections to the CGF for the 2SK model.

to the  $n$ th moment of charge current,

$$C_n^{\text{el}} = \frac{V^3}{12\pi} (-1)^n (\alpha_e - \alpha_o)^2. \quad (19)$$

We follow a procedure similar to that for the calculation of the scattering contribution to get the interaction correction to the CGF. Substituting the interaction (inelastic) part of the Hamiltonian,  $H_{\text{in}}$ , into Eq. (11) and applying Wick's theorem, we obtain the Feynman diagrams accounting for the interaction effect in the 2SK effect. These diagrams are shown in Fig. 4. We allocate these interaction correction diagrams into three topologically different classes, namely, type I1, type I2, and type I3, as shown in the bottom panel of Fig. 3. We introduce the notation  $\ln \chi_{ij}(\lambda)$  ( $j = 1, 2, 3$ ) to represent

the interaction correction to the CGF corresponding to the diagram of type Ij. The real-time GFs given in Eq. (17) pave the way for systematic calculation of  $\ln \chi_{ij}(\lambda)$ . As detailed in Appendix B, we write the type-I1 and type-I3 diagrammatic contribution to the CGF as

$$\ln \chi_{I1/I3} = \pm \frac{\Phi^2 \mathcal{T} V}{24\pi} \left[ \frac{V^2 + 4(\pi T)^2}{\sinh(V/2T)} \sum_{x=\pm} (e^{-i\lambda x} - 1) e^{xV/2T} \pm 2 \frac{V^2 + (\pi T)^2}{\sinh(V/T)} \sum_{x=\pm} (e^{-2i\lambda x} - 1) e^{xV/T} \right]. \quad (20)$$

Furthermore, the type-I2 diagram produces the interaction correction to the CGF as

$$\ln \chi_{I2} = \frac{\Phi^2 \mathcal{T} V}{12\pi} \frac{V^2 + (\pi T)^2}{\sinh(V/T)} \sum_{x=\pm} (e^{-2i\lambda x} - 1) e^{xV/T}. \quad (21)$$

Substituting Eqs. (20) and (21) into Eq. (12), we get the  $n$ th-order cumulant of the charge current,  $\mathcal{C}_n^{Ij}$ , corresponding to the type-Ij diagram. Of particular interest, the zero-temperature results are

$$\mathcal{C}_n^{I1/I3} = \pm \frac{V^3}{12\pi} (-1)^n [1 \pm 2^{n+1}] \Phi^2, \quad (22)$$

$$\mathcal{C}_n^{I2} = \frac{V^3}{12\pi} (-1)^n 2^{n+1} \Phi^2. \quad (23)$$

#### IV. RESULTS AND DISCUSSION

Collecting all the interaction contributions as detailed in Fig. 4, and the scattering contribution given in Eq. (19), we get the  $n$ th cumulant of the charge current at  $T = 0$  as

$$\mathcal{C}_n = (-1)^n \frac{V^3}{6\pi} (\alpha_e - \alpha_o)^2 [1 + 2^n \mathcal{L}], \quad (24)$$

with

$$\mathcal{L} \equiv 1 + 9\mathcal{Z}, \quad \mathcal{Z} = \frac{(\Phi - 2/3\alpha_e)(\Phi - 2/3\alpha_o)}{(\alpha_e - \alpha_o)^2}. \quad (25)$$

The parameter  $\mathcal{Z}$  signifies the lack of universality away from the symmetry point,  $\alpha_e = \alpha_o$  and  $\Phi = 2/3 \alpha_a$  of the 2SK Hamiltonian. In addition, it has been predicted that the parameter  $\mathcal{Z}$  is bounded such that  $-1/9 \leq \mathcal{Z} \leq 0$  [61]. For the sake of simplicity, we introduce the new parameter  $\mathcal{L}$  ( $\equiv 1 + 9\mathcal{Z}$ ) in such a way that  $0 \leq \mathcal{L} \leq 1$ . The minimum of  $\mathcal{L}$  corresponds to the exact symmetry between two channels at resonance. The case of infinite asymmetry between even and odd channels,  $T_K^o/T_K^e \rightarrow 0$ , is characterized by the upper bound of  $\mathcal{L}$ . This particular point, where the odd channel is decoupled from the impurity, recovers the 1CK paradigm. We see, from Eq. (24), that the  $n$ th cumulant of the charge current exactly vanishes at the symmetry point due to the destructive interference between the two resonance channels. The same result holds true even at finite temperature. However, l'Hôpital's rule permits us to have the finite value of the normalized  $n$ th cumulant,  $\mathcal{C}_n/\mathcal{C}_1$ . Then we define the measure of backscattering via the generalized Fano factor

$$F \equiv |\mathcal{C}_2/\mathcal{C}_1| = \frac{1 + 4\mathcal{L}}{1 + 2\mathcal{L}}. \quad (26)$$

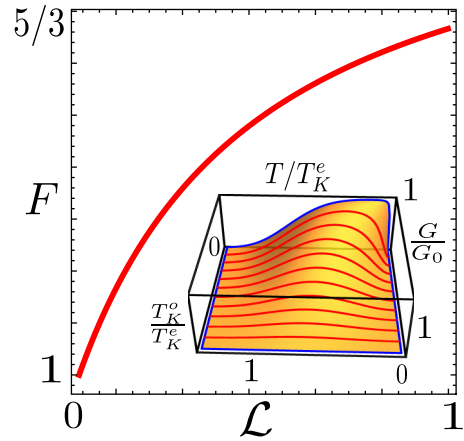


FIG. 5. The evolution of Fano factor ( $F$ ) as a function of channel-asymmetry parameter ( $\mathcal{L}$ ) for a generic 2SK effect. Inset: The nonmonotonic conductance behavior, the major hallmark of 2SK effect (see text for details).

Plugging the parameter  $\mathcal{L}$  into Eq. (26), we get the Fano factor bounded from above and below in such a way that  $1 \leq F \leq 5/3$ . The upper bound recoups the Fano factor of the 1CK effect, the super-Poissonian charge-transferred statistics [63]. The regime of maximum interaction in the 2SK effect results in the lower bound of  $F$ . This minimum of  $F$  ( $= 1$ ) represents the Poissonian regime of charge distribution. Therefore, a generic 2SK effect exhibits the crossover regime of charge-transferred statistics, from Poissonian to super-Poissonian, depending upon the channel asymmetry. This *monotonic* dependence of  $F$  on the channel-asymmetry parameter  $\mathcal{L}$  is shown in Fig. 5. The *nonmonotonic* conductance of the 2SK effect as a function of temperature, extracted from  $\mathcal{C}_1|_{T \neq 0, V \rightarrow 0}$ , is shown in the inset of Fig. 5 (see Ref. [61] for a detailed description).

In 1CK schemes, the definition of the generalized Fano factor follows from  $F \equiv \delta\mathcal{C}_2/\delta\mathcal{C}_1|_{T \rightarrow 0}$ , where  $\delta\mathcal{C}_{1/2}$  represents the corresponding quantity after subtracting the linear part (those terms  $\propto V$ ). Nevertheless, the  $n$ th cumulant of the charge current in 2SK schemes, Eq. (24), does not show the linear terms in  $V$ . This makes for a very straightforward extraction of  $F$  in the 2SK effect, since it does not require the proper subtraction of linear terms.

The differential conductance of the 2SK effect as a function of  $B$  (the Zeeman field),  $T$ , and  $V$  is given, in terms of FL transport coefficients, as  $G/G_0 = c_B B^2 + c_T (\pi T)^2 + c_V V^2$ , where  $G_0$  is the unitary conductance. The transport coefficients bear the compact form:  $c_T/c_B = (\mathcal{L} + 2)/3$  and  $c_V/c_B = \mathcal{L} + 1/2$  [61]. Thus, the measurement of  $\mathcal{L}$  would suffice in the study of transport behaviors of the 2SK effect. The compelling monotonic dependence of  $F$  on  $\mathcal{L}$ , as shown in Fig. 5, could furnish an experimental way to extract  $\mathcal{L}$  as follows. Given an experimental setup in the 2SK scheme, the independent measurements of charge current and noise impart the Fano factor. Thus obtained, the Fano factor uniquely defines the corresponding asymmetry parameter  $\mathcal{L}$  via Eq. (5). Following this way of measuring transport coefficients could be less involved than measuring the response functions.

## V. CONCLUSION

We extended the FCS method from conventional 1CK schemes to the multichannel Kondo paradigm. The developed framework of the FCS has been demonstrated considering an example of the 2SK effect. We analyzed the charge-transferred statistics in the strong-coupling regime of a 2SK model using a nonequilibrium Keldysh formulation. We found that the arbitrary cumulant of the charge current gets nullified at the symmetry point of the 2SK model due to the destructive interference between the two conducting channels. We studied the destructiveness and constructiveness of interference in terms of the channel asymmetry parameter,  $\mathcal{L}$ . The  $n$ th-order normalized cumulant of the charge current,  $C_n/C_1$ , took a compact function of  $\mathcal{L}$  only. A bounded value of the Fano factor,  $1 \leq F \leq 5/3$ , has been discovered. Studying the observed monotonic growth of  $F$  as a function of  $\mathcal{L}$ , we uncovered the crossover regimes of charge-transferred statistics in the 2SK effect, from Poissonian to super-Poissonian. We proposed a way of obtaining the FL transport coefficients of the 2SK effect by the independent measurements of charge current and noise. The developed formalism imparts all the transport information of the 1CK effect as well. All the calculations have been performed at finite temperature; one can easily study the effect of temperature on an arbitrary cumulant of the charge current [66].

## ACKNOWLEDGMENTS

We benefited from illuminating discussions with Jan van Delft and Christophe Mora at the early stage of this project. We are thankful to Michele Fabrizio, Leonid Glazman, Yuval Oreg, Felix von Oppen, Achim Rosch, and Eran Sela for fruitful discussions.

## APPENDIX A: SCATTERING CORRECTIONS TO THE CGF

The scattering correction to the MGF of the 2SK model reads

$$\chi_{\text{el}}(\lambda) = \left\langle T_C \exp \left[ -i \int_C \mathcal{H}_{\text{el}}^\lambda(t) dt \right] \right\rangle_0, \quad (\text{A1})$$

where the scattering Hamiltonian is given in Eq. (5). The logarithm of Eq. (A1),  $\ln \chi_{\text{el}}(\lambda)$ , imparts the corresponding CGF. The second-order expansion of  $\ln \chi_{\text{el}}(\lambda)$  in  $\mathcal{H}_{\text{el}}^\lambda$  followed by the use of Wick's theorem results in four different Feynman diagrams as shown in Fig. 3 (top). The first and second diagrams are composed of only the channel-diagonal GFs. Owing to their similar geometry, we classified them as type-E1 diagrams. Note that, in our convention, the two diagrams are geometrically similar if they contain an equal number of channel-diagonal GFs (if present) and an equal number of mixed GFs (if present). The type-E2 diagrams shown in Fig. 3, nonetheless, consist of only mixed GFs. The interference between two channels, due to the scattering effects, is accounted for by these type-E2 diagrams. The contribution of type-E1 diagrams to the CGF is proportional to  $\alpha_a^2$ . Similarly, the CGF contribution of type-E2 diagrams is proportional to  $\alpha_a \alpha_{\bar{a}}$ . Therefore, the overall scattering contribution to CGF is

written as

$$\ln \chi_{\text{el}} = \sum_a \left( \ln \chi_{\alpha_a^2} + \ln \chi_{\alpha_a \alpha_{\bar{a}}} \right). \quad (\text{A2})$$

Topologically the type-E1 and type-E2 diagrams are quite distinct. The type-E1 diagram has already appeared in several previous works [49,50,52–54]; however, the type-E2 diagram has not been considered yet. For completeness, we present the mathematical details of the diagrammatic contribution to the CGF for both diagrams. For type-E1 diagrams we write

$$\begin{aligned} \ln \chi_{\alpha_a^2} = & -\frac{1}{2} \frac{\alpha_a^2}{(2\pi\nu)^2} \sum_{kk'\sigma} \sum_{pp'\sigma'} (\varepsilon_k + \varepsilon_{k'}) (\varepsilon_p + \varepsilon_{p'}) \\ & \times \int_C dt_1 dt_2 \langle T_C b_{ak\sigma}^\dagger(t_1) b_{ak'\sigma}(t_1) b_{ap'\sigma'}^\dagger(t_2) b_{ap'\sigma'}(t_2) \rangle. \end{aligned} \quad (\text{A3})$$

Here, we introduced the set of momentum indices ( $k, k', p, p'$ ), spin indices ( $\sigma, \sigma'$ ), and time indices ( $t_1, t_2$ ). Equation (A3) imparts the nonzero contribution only if  $k = p', k' = p$ , and  $\sigma = \sigma'$ . Therefore, use of the method of Keldysh disentanglement in Eq. (A3) results in

$$\begin{aligned} \ln \chi_{\alpha_a^2} = & -\frac{1}{2} \frac{\alpha_a^2 \mathcal{T}}{(2\pi\nu)^2} \sum_{kk'\sigma} (\varepsilon_k + \varepsilon_{k'})^2 \\ & \times \sum_{\eta_1 \eta_2} \eta_1 \eta_2 \int_C dt \mathcal{G}_{aa,k'\sigma}^{\eta_1 \eta_2}(t) \mathcal{G}_{aa,k\sigma}^{\eta_2 \eta_1}(-t), \end{aligned} \quad (\text{A4})$$

where  $\mathcal{T}$  is the measurement time (see Sec. III), and  $\eta_i$  ( $i = 1, 2$ ) are the Keldysh branch (forward and backward) indices such that  $\eta_i = \pm 1$ . The channel-diagonal GFs,  $\mathcal{G}_{aa}^{\eta_1 \eta_2}$ , are defined in Eqs. (14)–(16). These GFs acquire the special property  $\nu \mathcal{G}_{aa,k\sigma}^{\eta_1 \eta_2}(\varepsilon) = \mathcal{G}_{aa,\sigma}^{\eta_1 \eta_2}(\varepsilon) \delta(\varepsilon - \varepsilon_k)$ , where  $\delta(\varepsilon - \varepsilon_k)$  stands for the Kronecker delta. Then, Eq. (A4) reads

$$\ln \chi_{\alpha_a^2} = -\frac{1}{2} \frac{\alpha_a^2 \mathcal{T}}{(\pi\nu)^2} \sum_{\eta_1 \eta_2, \sigma} \eta_1 \eta_2 \int_C \frac{d\varepsilon}{2\pi} \varepsilon^2 \mathcal{G}_{aa,\sigma}^{\eta_1 \eta_2}(\varepsilon) \mathcal{G}_{aa,\sigma}^{\eta_2 \eta_1}(\varepsilon). \quad (\text{A5})$$

Summing Eq. (A5) over  $\eta_{1/2}$  and then plugging in the various Keldysh GFs from Eqs. (14)–(16) leads to

$$\ln \chi_{\alpha_a^2} = \frac{\alpha_a^2 \mathcal{T}}{2\pi} \sum_{\sigma} \mathcal{J}_{\text{el},\sigma}, \quad (\text{A6})$$

with the compact form of the integral characterizing the scattering effects,

$$\mathcal{J}_{\text{el}} = \int_{-\infty}^{\infty} \varepsilon^2 d\varepsilon [f_S(1-f_D)(e^{-i\lambda}-1) + f_D(1-f_S)(e^{i\lambda}-1)]. \quad (\text{A7})$$

We called this integral the ‘‘elastic integral’’; the mathematical details of its computation are discussed in Appendix C.

Repeating all the above calculations for type-E2 diagrams with the same notation, we get the quite similar result

$$\ln \chi_{\alpha_a \alpha_{\bar{a}}} = -\frac{\alpha_a \alpha_{\bar{a}} \mathcal{T}}{2\pi} \sum_{\sigma} \mathcal{J}_{\text{el},\sigma}. \quad (\text{A8})$$

Though the origins of these two elastic diagrams and corresponding topology are quite distinct, it turns out that they produce equal but opposite contributions to the CGF. Plugging Eqs. (A6) and (A8) into Eq. (A2) imparts the contribution of scattering effects to the CGF, which is written as

$$\ln \chi_{el} = \frac{(\alpha_e - \alpha_0)^2 \mathcal{T}}{2\pi} \sum_{\sigma} \mathcal{J}_{el,\sigma}. \quad (\text{A9})$$

Substituting the value of the elastic integral from Eq. (C10) into Eq. (A9), we get the final expression for the scattering contribution to the CGF in the 2SK model, which is Eq. (18) in the main text of this paper.

## APPENDIX B: INTERACTION CORRECTIONS TO THE CGF

In the same way and using the same notation as for the scattering contribution, we get several Feynman diagrams contributing to the CGF of the 2SK model as shown in Fig. 4. These diagrams are classified into three different groups: type Ij (where j=1, 2, 3) diagrams, based upon the numbers of channel-diagonal GFs and mixed GFs present in a particular diagram (see the bottom of Fig. 3). For instance, the diagram with all (four) channel-diagonal GFs has been classified as a type-I1 diagram, those with two channel-diagonal and the remaining two mixed GFs as type I2, and diagrams with all mixed GFs as type I3. As detailed in Fig. 4, we expressed the interaction contribution to the CGF in terms of these three diagrams. The two diagrams belonging to the same group might have different weight factors. The numbers of close fermion loops, the product of Pauli matrices, and the renormalization factor in the Hamiltonian determines the weight factor corresponding to a particular diagram (for detail see Ref. [61]).

A single diagram of type I1 (with CGF contribution proportional to  $\phi_{e/o}^2$ ) completely characterizes the FCS of the 1CK schemes [49,50,52–54]. However, the type-I2 and type-I3 diagrams are generic features of multichannel, multistage screening effects. These diagrams have not been studied yet. In this Appendix we provide the mathematical details of computing the CGF contribution of type-Ij diagrams.

The type-I1 diagram shown in the bottom of Fig. 3 produces a CGF contribution proportional to  $\Phi^2$ . Following the standard technique of Feynman diagram calculation, we cast the CGF contribution of the type-I1 diagram into the form

$$\ln \chi_{I1} = -\frac{1}{2} \left( \frac{\Phi}{\pi v} \right)^2 \int_C dt_1 dt_2 [\mathcal{G}_{ee,\sigma}(t_1 - t_2) \mathcal{G}_{ee,\sigma}(t_2 - t_1) \times \mathcal{G}_{oo,\sigma}(t_1 - t_2) \mathcal{G}_{oo,\sigma}(t_2 - t_1)]. \quad (\text{B1})$$

In Eq. (B1) we did not consider the spin summation for being more general (implying that the spin index  $\sigma$  is either down or up). Using the technique of Keldysh disentanglement we write Eq. (B1) as

$$\ln \chi_{I1} = -\frac{\mathcal{T}}{2} \left( \frac{\Phi}{\pi v} \right)^2 \sum_{\eta_1 \eta_2} \eta_1 \eta_2 \times \int_C dt [\mathcal{G}_{ee,\sigma}^{\eta_1 \eta_2}(t) \mathcal{G}_{ee,\sigma}^{\eta_2 \eta_1}(-t) \mathcal{G}_{oo,\sigma}^{\eta_1 \eta_2}(t) \mathcal{G}_{oo,\sigma}^{\eta_2 \eta_1}(-t)]. \quad (\text{B2})$$

Summing Eq. (B2) over Keldysh indices  $\eta_{1/2}$  and using the expressions of GFs in Eq. (17), we get

$$\ln \chi_{I1} = (\pi \Phi T^2)^2 \mathcal{T} \int_{-\infty+i\gamma}^{\infty+i\gamma} \frac{\cos^4(\frac{\lambda}{2} + \frac{v}{2}t)}{\sinh^4(\pi T t)} dt. \quad (\text{B3})$$

Coming from Eq. (B1) to Eq. (B3), we retain only the  $\lambda$ -dependent terms. The integral involved in Eq. (B3) is computed in Appendix D. Then we write the CGF contribution of the type-I1 diagram in the form

$$\ln \chi_{I1} = \frac{\Phi^2 \mathcal{T}}{96\pi} \left[ \frac{8V(V^2 + (\pi T)^2)}{\sinh(V/T)} \sum_{x=\pm} e^{2ix\lambda} e^{-xV/T} \times \frac{4V(V^2 + 4(\pi T)^2)}{\sinh(V/2T)} \sum_{x=\pm} e^{ix\lambda} e^{-xV/2T} \right] + \frac{\pi \Phi^2 T^3 \mathcal{T}}{2}. \quad (\text{B4})$$

For proper renormalization of the PDF we subtract the  $\lambda = 0$  contribution of Eq. (B4) from the same Eq. (B4), which results in the final expression of CGF contributed by a diagram of type I1:

$$\ln \chi_{I1} = \frac{\Phi^2 \mathcal{T} V}{24\pi} \left[ 2 \frac{V^2 + (\pi T)^2}{\sinh(V/T)} \sum_{x=\pm} (e^{2ix\lambda} - 1) e^{-xV/T} + \frac{V^2 + 4(\pi T)^2}{\sinh(V/2T)} \sum_{x=\pm} (e^{ix\lambda} - 1) e^{-xV/2T} \right]. \quad (\text{B5})$$

In the same way and using the same notation as for the type-I1 diagram, the CGF contribution of the type-I2 diagram as shown in Fig. 3 reads

$$\ln \chi_{I2} = -(\pi \Phi T^2)^2 \mathcal{T} \int_{-\infty+i\gamma}^{\infty+i\gamma} \frac{\sin^2(\frac{\lambda}{2} + \frac{v}{2}t) \cos^2(\frac{\lambda}{2} + \frac{v}{2}t)}{\sinh^4(\pi T t)} dt. \quad (\text{B6})$$

Using the integral given in Appendix D followed by the proper renormalization of the PDF, Eq. (B6) results in

$$\ln \chi_{I2} = \frac{\Phi^2 \mathcal{T} V}{12\pi} \frac{V^2 + (\pi T)^2}{\sinh(V/T)} \sum_{x=\pm} (e^{2ix\lambda} - 1) e^{-xV/T}. \quad (\text{B7})$$

Similarly, the CGF contribution of a type-I3 diagram as shown in Fig. 3 is given by

$$\ln \chi_{I3} = (\pi \Phi T^2)^2 \mathcal{T} \int_{-\infty+i\gamma}^{\infty+i\gamma} \frac{\sin^4(\frac{\lambda}{2} + \frac{v}{2}t)}{\sinh^4(\pi T t)} dt. \quad (\text{B8})$$

The simplification of Eq. (B8) upon proper renormalization of the PDF imparts

$$\ln \chi_{I3} = -\frac{\Phi^2 \mathcal{T} V}{24\pi} \left[ \frac{V^2 + 4(\pi T)^2}{\sinh(V/2T)} \sum_{x=\pm} (e^{ix\lambda} - 1) e^{-xV/2T} - 2 \frac{V^2 + (\pi T)^2}{\sinh(V/T)} \sum_{x=\pm} (e^{2ix\lambda} - 1) e^{-xV/T} \right]. \quad (\text{B9})$$

## APPENDIX C: ELASTIC INTEGRAL

This section contains the details of the calculation of the elastic integral in Eq. (A7) using the properties of FT. First

we factorized the elastic integral as

$$\mathcal{J}_{\text{el}} = (e^{-i\lambda} - 1)\mathcal{J}_{\text{el}}^1 + (e^{i\lambda} - 1)\mathcal{J}_{\text{el}}^2. \quad (\text{C1})$$

Here, we introduced the shorthand notation

$$\mathcal{J}_{\text{el}}^1 = \int_{-\infty}^{\infty} \varepsilon^2 d\varepsilon f_S(1-f_D), \quad \mathcal{J}_{\text{el}}^2 = \int_{-\infty}^{\infty} \varepsilon^2 d\varepsilon f_D(1-f_S). \quad (\text{C2})$$

At  $T = 0$  we have  $f_{S/D}(\varepsilon) = \Theta(\mu_{S/D} - \varepsilon)$  and  $1 - f_{S/D}(\varepsilon) = \Theta(\varepsilon - \mu_{S/D})$ . Thus the zero-temperature limit of Eq. (C1) is quite trivial:

$$\mathcal{J}_{\text{el}}|_{T=0} = (e^{-i\lambda} - 1) \int_{\mu_R}^{\mu_L} \varepsilon^2 d\varepsilon = (e^{-i\lambda} - 1) \frac{V^3}{12}. \quad (\text{C3})$$

However, the Fermi distribution functions of the source and drain, and their FT at finite temperature, are

$$f_{S/D}(\varepsilon) = \frac{e^{-(\varepsilon - \mu_{S/D})/2T}}{2 \cosh[(\varepsilon - \mu_{S/D})/2T]};$$

$$f_{S/D}(t) = \frac{iT}{2} \frac{e^{-it\mu_{S/D}}}{\sinh(\pi T t)}. \quad (\text{C4})$$

For the sake of simplicity we define another function  $h_{L/R}(\varepsilon)$  and its FT as

$$h_{S/D}(\varepsilon) = e^{-\frac{\varepsilon}{T}} f_{S/D}(\varepsilon), \quad h_{S/D}(t) = -\frac{iT}{2} \frac{e^{-it\mu_{S/D} - \frac{\mu_{S/D}}{T}}}{\sinh(\pi T t)}. \quad (\text{C5})$$

The function  $h_{S/D}(\varepsilon)$  in Eq. (C5) paves the way to convert the product of Fermi functions into a weighted sum. For instance,

$$f_S(\varepsilon)f_D(\varepsilon) = \frac{h_S(\varepsilon) - h_D(\varepsilon)}{e^{-\frac{\mu_D}{T}} - e^{-\frac{\mu_S}{T}}} = \frac{h_S(\varepsilon) - h_D(\varepsilon)}{2 \sinh(V/2T)}. \quad (\text{C6})$$

Then,  $\mathcal{J}_{\text{el}}^1$  and  $\mathcal{J}_{\text{el}}^2$  simplify to

$$\mathcal{J}_{\text{el}}^{1/2} = \int_{-\infty}^{\infty} \varepsilon^2 d\varepsilon f_{S/D}(\varepsilon) - \frac{\int_{-\infty}^{\infty} \varepsilon^2 d\varepsilon [h_L(\varepsilon) - h_R(\varepsilon)]}{2 \sinh(V/2T)}. \quad (\text{C7})$$

Having defined the FT of the functions  $f_{S/D}$  and  $h_{S/D}$ , we performed the integration of Eq. (C7) by using the property of FT [61],

$$\int_{-\infty}^{\infty} \varepsilon^n y(\varepsilon) d\varepsilon = \frac{2\pi}{(-i)^n} \partial_t^n [y(t)]|_{t=0}. \quad (\text{C8})$$

Here,  $y(\varepsilon)$  is an arbitrary function with FT  $y(t)$  and  $\partial_t^n$  represents the  $n$ th-order differentiation with respect to  $t$ . Substitution of Eq. (C8) for  $n = 2$  into Eq. (C7) and then using the definitions of  $f_{S/D}(t)$  and  $h_{S/D}(t)$  defined in Eqs. (C4) and (C5) lead the result

$$\mathcal{J}_{\text{el}}^{1/2} = \pm \frac{V}{2} \left[ \frac{(\pi T)^2}{3} + \frac{V^2}{12} \right] \left[ 1 \pm \coth\left(\frac{V}{2T}\right) \right]. \quad (\text{C9})$$

Plugging in  $\mathcal{J}_{\text{el}}^{1/2}$  from Eq. (C9) into Eq. (C1), we obtain the final expression for the elastic integral:

$$\mathcal{J}_{\text{el}} = \frac{V}{24} \frac{V^2 + 4(\pi T)^2}{\sinh(V/2T)} [(e^{-i\lambda} - 1)e^{V/2T} + (e^{i\lambda} - 1)e^{-V/2T}]. \quad (\text{C10})$$

This is the central equation governing the CGF contribution of scattering effects in the 2SK model.

#### APPENDIX D: INELASTIC INTEGRAL

For the computation of integrals in Eqs. (B3), (B6), and (B8), we expand their numerators in powers of  $e^{\pm i(\lambda/2 + Vt/2)}$ . Each term gives an integral of the form

$$\mathcal{I}_{\pm} = \int_{-\infty + i\gamma}^{\infty + i\gamma} \frac{e^{\pm iAt}}{\sinh^4(\pi T t)} dt, \quad A > 0. \quad (\text{D1})$$

The singularity of the integral in Eq. (D1) is removed by shifting the time contour by  $i\gamma$  in the complex plane such that  $\gamma D \gg 1$ ,  $\gamma T \ll 1$ , and  $\gamma A \ll 1$ . Here,  $D$  is the band cutoff. The poles of the integrand of  $\mathcal{I}_{\pm}$  are given by the solution of  $\sinh(\pi T t) = 0$  for  $t$ , which leads to

$$\pi T t = \pm im\pi \Rightarrow t = \pm \frac{im}{T}, \quad m = 0, \pm 1, \pm 2, \pm 3, \dots$$

With the choice of the rectangular contour shifted by  $i/T$  in the complex plane which includes the pole of the integrand at  $t = 0$ , the standard method of complex integration results in

$$\mathcal{I}_{+}(1 - e^{A/T}) = -2\pi i \times \text{Res}|_{t=0}, \quad (\text{D2})$$

where  $\text{Res}|_{t=0}$  stands for the Cauchy residue of the integrand in Eq. (D1) at  $t = 0$ . Plugging the residue into Eq. (D2) results in

$$\mathcal{I}_{+} = -\frac{2\pi(\mathcal{A}^3 + 4\mathcal{A}(\pi T)^2)}{6(\pi T)^4} \frac{1}{1 - e^{\frac{\mathcal{A}}{T}}}. \quad (\text{D3})$$

Similarly we computed  $\mathcal{I}_{-}$ . The integrals  $\mathcal{I}_{\pm}$  are sufficient for the computation of all the inelastic diagrams shown in Fig. 4.

[1] Y. Blanter and M. Buttiker, *Phys. Rep.* **336**, 1 (2000).  
[2] Y. M. Blanter and Y. V. Nazarov, *Quantum Transport: Introduction to Nanoscience* (Cambridge University Press, Cambridge, UK, 2009).  
[3] L. S. Levitov and G. B. Lesovik, *Pis'ma Zh. Eksp. Teor. Fiz.* **58**, 225 (1993) [*JETP Lett.* **58**, 230 (1993)].  
[4] H. Lee, L. S. Levitov, and A. Y. Yakovets, *Phys. Rev. B* **51**, 4079 (1995).

[5] L. S. Levitov, H. Lee, and G. B. Lesovik, *J. Math. Phys.* **37**, 4845 (1996).  
[6] L. S. Levitov, *Quantum Noise in Mesoscopic Systems*, edited by Y. V. Nazarov (Kluwer, Dordrecht, 2003).  
[7] D. A. Bagrets and Y. V. Nazarov, *Phys. Rev. B* **67**, 085316 (2003).  
[8] L. S. Levitov and M. Reznikov, *Phys. Rev. B* **70**, 115305 (2004).

- [9] S. Gustavsson, R. Leturcq, B. Simovič, R. Schleser, T. Ihn, P. Studerus, K. Ensslin, D. C. Driscoll, and A. C. Gossard, *Phys. Rev. Lett.* **96**, 076605 (2006).
- [10] W. Belzig, *Phys. Rev. B* **71**, 161301 (2005).
- [11] A. A. Clerk, M. H. Devoret, S. M. Girvin, F. Marquardt, and R. J. Schoelkopf, *Rev. Mod. Phys.* **82**, 1155 (2010).
- [12] B. Reulet, J. Senzier, and D. E. Prober, *Phys. Rev. Lett.* **91**, 196601 (2003).
- [13] Y. Bomze, G. Gershon, D. Shovkun, L. S. Levitov, and M. Reznikov, *Phys. Rev. Lett.* **95**, 176601 (2005).
- [14] T. Fujisawa, T. Hayashi, R. Tomita, and Y. Hirayama, *Science* **312**, 1634 (2006).
- [15] C. Fricke, F. Hohls, W. Wegscheider, and R. J. Haug, *Phys. Rev. B* **76**, 155307 (2007).
- [16] A. V. Timofeev, M. Meschke, J. T. Peltonen, T. T. Heikkilä, and J. P. Pekola, *Phys. Rev. Lett.* **98**, 207001 (2007).
- [17] G. Gershon, Y. Bomze, E. V. Sukhorukov, and M. Reznikov, *Phys. Rev. Lett.* **101**, 016803 (2008).
- [18] J. Gabelli and B. Reulet, *Phys. Rev. B* **80**, 161203 (2009).
- [19] C. Flindt, C. Fricke, F. Hohls, T. Novotný, K. Netočný, T. Brandes, and R. J. Haug, *Proc. Natl. Acad. Sci. USA* **106**, 10116 (2009).
- [20] B. A. Muzykantskii and D. E. Khmel'nitskii, *Phys. Rev. B* **50**, 3982 (1994).
- [21] W. Belzig and Y. V. Nazarov, *Phys. Rev. Lett.* **87**, 067006 (2001).
- [22] S. Pilgram, A. N. Jordan, E. V. Sukhorukov, and M. Büttiker, *Phys. Rev. Lett.* **90**, 206801 (2003).
- [23] F. Taddei and R. Fazio, *Phys. Rev. B* **65**, 075317 (2002).
- [24] A. Di Lorenzo and Y. V. Nazarov, *Phys. Rev. Lett.* **93**, 046601 (2004).
- [25] A. Braggio, J. König, and R. Fazio, *Phys. Rev. Lett.* **96**, 026805 (2006).
- [26] F. Pistolesi, *Phys. Rev. B* **69**, 245409 (2004).
- [27] S. D. Bennett and A. A. Clerk, *Phys. Rev. B* **78**, 165328 (2008).
- [28] D. Kambly, C. Flindt, and M. Büttiker, *Phys. Rev. B* **83**, 075432 (2011).
- [29] A. Hewson, *The Kondo Problem to Heavy Fermions* (Cambridge University Press, Cambridge, UK, 1993).
- [30] P. Coleman, *Introduction to Many-Body Physics* (Cambridge University Press, Cambridge, UK, 2015).
- [31] D. L. Cox and A. Zawadowski, *Adv. Phys.* **47**, 599 (1998).
- [32] J. Kondo, *Prog. Theor. Phys.* **32**, 37 (1964).
- [33] P. Nozières, *J. Low Temp. Phys.* **17**, 31 (1974).
- [34] P. Nozières and A. Blandin, *J. Phys.* **41**, 193 (1980).
- [35] I. Affleck and A. W. W. Ludwig, *Phys. Rev. B* **48**, 7297 (1993).
- [36] N. E. Bickers, D. L. Cox, and J. W. Wilkins, *Phys. Rev. Lett.* **54**, 230 (1985).
- [37] D. Goldhaber-Gordon, H. Shtrikman, D. Mahalu, D. Abusch-Magder, U. Meirav, and M. A. Kastner, *Nature (London)* **391**, 156 (1998).
- [38] S. M. Cronenwett, T. H. Oosterkamp, and L. P. Kouwenhoven, *Science* **281**, 540 (1998).
- [39] J. Nygård, D. H. Cobden, and P. E. Lindelof, *Nature (London)* **408**, 342 (2000).
- [40] L. Kouwenhoven and L. Glazman, *Phys. World* **14**, 33 (2001).
- [41] S. Jezouin, F. D. Parmentier, A. Anthore, U. Gennser, A. Cavanna, Y. Jin, and F. Pierre, *Science* **342**, 601 (2013).
- [42] A. J. Keller, S. Amasha, I. Weymann, C. P. Moca, I. G. Rau, J. A. Katine, H. Shtrikman, G. Zaránd, and D. Goldhaber-Gordon, *Nat. Phys.* **10**, 145 (2014).
- [43] Z. Iftikhar, S. Jezouin, A. Anthore, U. Gennser, F. D. Parmentier, A. Cavanna, and F. Pierre, *Nature (London)* **526**, 233 (2015).
- [44] S. Jezouin, Z. Iftikhar, A. Anthore, F. D. Parmentier, U. Gennser, A. Cavanna, A. Ouerghi, I. P. Levkivskiy, E. Idrisov, E. V. Sukhorukov, L. I. Glazman, and F. Pierre, *Nature (London)* **536**, 60 (2016).
- [45] M. Pustilnik and L. Glazman, *J. Phys.: Condens. Matter* **16**, R513 (2004).
- [46] C. Mora, X. Leyronas, and N. Regnault, *Phys. Rev. Lett.* **100**, 036604 (2008).
- [47] C. Mora, P. Vitushinsky, X. Leyronas, A. A. Clerk, and K. Le Hur, *Phys. Rev. B* **80**, 155322 (2009).
- [48] M. Hanl, A. Weichselbaum, J. von Delft, and M. Kiselev, *Phys. Rev. B* **89**, 195131 (2014).
- [49] A. O. Gogolin and A. Komnik, *Phys. Rev. Lett.* **97**, 016602 (2006).
- [50] A. O. Gogolin and A. Komnik, *Phys. Rev. B* **73**, 195301 (2006).
- [51] A. Golub, *Phys. Rev. B* **73**, 233310 (2006).
- [52] T. L. Schmidt, A. O. Gogolin, and A. Komnik, *Phys. Rev. B* **75**, 235105 (2007).
- [53] T. L. Schmidt, A. Komnik, and A. O. Gogolin, *Phys. Rev. B* **76**, 241307 (2007).
- [54] R. Sakano, Y. Nishikawa, A. Oguri, A. C. Hewson, and S. Tarucha, *Phys. Rev. Lett.* **108**, 266401 (2012).
- [55] M. Pustilnik and L. I. Glazman, *Phys. Rev. Lett.* **87**, 216601 (2001).
- [56] S. Sasaki, S. De Franceschi, J. M. Elzerman, W. G. van der Wiel, M. Eto, S. Tarucha, and L. P. Kouwenhoven, *Nature (London)* **405**, 764 (2000).
- [57] M. Eto and Y. V. Nazarov, *Phys. Rev. Lett.* **85**, 1306 (2000).
- [58] C. H. L. Quay, J. Cumings, S. J. Gamble, R. de Picciotto, H. Kataura, and D. Goldhaber-Gordon, *Phys. Rev. B* **76**, 245311 (2007).
- [59] A. K. Mitchell, K. G. L. Pedersen, P. Hedegard, and J. Paaske, *Nat. Commun.* **8**, 15210 (2017).
- [60] A. Posazhennikova and P. Coleman, *Phys. Rev. Lett.* **94**, 036802 (2005).
- [61] D. B. Karki, C. Mora, J. von Delft, and M. N. Kiselev, *Phys. Rev. B* **97**, 195403 (2018).
- [62] A. Posazhennikova, B. Bayani, and P. Coleman, *Phys. Rev. B* **75**, 245329 (2007).
- [63] E. Sela, Y. Oreg, F. von Oppen, and J. Koch, *Phys. Rev. Lett.* **97**, 086601 (2006).
- [64] J. R. Schrieffer and P. Wolf, *Phys. Rev.* **149**, 491 (1966).
- [65] D. B. Karki and M. N. Kiselev, *Phys. Rev. B* **96**, 121403(R) (2017).
- [66] One can study the evolution of Fano factor as a function of  $V/T$  and the asymmetry parameter  $\mathcal{L}$  similar to that of Ref. [46] devoted to the 1CK effect.